ChemComm

Elucidating Ultrafast Electron Dynamics at Surfaces Using Extreme Ultraviolet (XUV) Reflection-Absorption Spectroscopy

Journal:	*ChemComm*
Manuscript ID	CC-FEA-03-2018-001745.R1
Article Type:	Feature Article

Journal Name

ARTICLE TYPE

Cite this: DOI: 10.1039/xxxxxxxxxx

Elucidating Ultrafast Electron Dynamics at Surfaces Using Extreme Ultraviolet (XUV) Reflection-Absorption Spectroscopy

Somnath Biswas†, Jakub Husek†, and L. Robert Baker*

Received Date
Accepted Date

DOI: 10.1039/xxxxxxxxxx

www.rsc.org/journalname

Here we review the recent development of extreme ultraviolet reflection-absorption (XUV-RA) spectroscopy. This method combines the benefits of X-ray absorption spectroscopy, such as element, oxidation, and spin state specificity, with surface sensitivity and ultrafast time resolution, having a probe depth of only a few nm and an instrument response less than 100 fs. Using this technique we investigated the ultrafast electron dynamics at a hematite (α-Fe_2O_3) surface. Surface electron trapping and small polaron formation both occur in 660 fs following photoexcitation. These kinetics are independent of surface morphology indicating that electron trapping is not mediated by defects. Instead, small polaron formation is proposed as the likely driving force for surface electron trapping. We also show that in Fe_2O_3, Co_3O_4, and NiO, band gap excitation promotes electron transfer from O 2p valence band states to metal 3d conduction band states. In addition to detecting the photoexcited electron at the metal $M_{2,3}$-edge, the valence band hole is directly observed as transient signal at the O L_1-edge. The size of the resulting charge transfer exciton is on the order of a single metal-oxygen bond length. Spectral shifts at the O L_1-edge correlate with metal-oxygen bond covalency, confirming the relationship between valence band hybridization and the overpotential for water oxidation. These examples demonstrate the unique ability to measure ultrafast electron dynamics with element and chemical state resolution using XUV-RA spectroscopy. Accordingly, this method is poised to play an important role to reveal chemical details of previously unseen surface electron dynamics.

1 Introduction

1.1 Surface Electron Dynamics

Surface electron dynamics play an important role in energy conversion processes.[1–3] For example, photovoltaics operate by charge separation across a heterojunction to produce a current,[4,5] while photo- and electrocatalysts rely on charge injection at a catalyst/reactant interface to drive a surface chemical reaction.[6–9] In many systems of current interest the early events leading to energy conversion are driven directly by light, making the study of photoinduced electron dynamics especially relevant for understanding the mechanisms and material properties governing device efficiency.[10–14] In such cases it is the time evolution of excited states that mediates energy transfer and drives eventual charge separation. When well controlled, these dynamics form the basis for efficient solar energy conversion such as in real[15–17] and artificial[16,18,19] photosynthetic systems, photovoltaics,[1,11,20] and photocatalysts.[7,21,22] However, processes such as carrier thermalization,[23,24] exciton recombination,[25,26] charge trapping,[7,27] and photodegradation[28,29] represent fundamental limits on device efficiency, making the fields of photochemistry and photophysics inseparably connected with the advancement of energy conversion applications.

Much work has been done in the field of molecular photochemistry, which provides a fundamental framework for understanding light-driven chemistry in molecules.[30–33] This work has extended to solid-state materials as well; however, in contrast to individual molecules, solids have a complicated electronic band structure that can be difficult to predict theoretically[34,35] and challenging to probe experimentally. Additionally, unlike molecules, solids are inherently heterogeneous. This is especially true of the surface electronic structure, which can vary greatly from the bulk electronic structure due to under-coordination,[36,37] interface bonding,[38,39] and chemical and structural defects.[40,41] In many cases defects states form exclusively at a surface, for example in the case of oxygen vacancy defects, which serve as n-type donors and electron trap states at the surface of many metal oxide semiconductors.[42,43] In other cases impurity induced defect states tend to segregate to a surface or interface.[44,45]

The Ohio State University, Columbus, OH, 43210, USA, E-mail: baker.2364@osu.edu
† *These authors contributed equally.*

Due to this complexity associated with surface chemistry and surface electronic structure, more is currently understood about molecular photophysics and reaction dynamics by comparison to solids. Using a variety of spectroscopic probes, it is possible to follow molecular photophysics with chemical detail, and reviews have been written describing charge, spin, and structural dynamics in a large range of molecular chromophores and photocatalysts.[46–49] Unfortunately, this level of detailed understanding is often lacking with regards to analogous processes occurring on solid surfaces due to the challenges associated with probing surfaces selectively with sensitivity to oxidation state, spin state, lattice distortions, electron-phonon coupling and carrier thermalization. Accordingly, surface photochemistry represents a challenging frontier with relevance to numerous catalytic and energy conversion processes. Because the advancement of many technologies relies on the ability to understand surface electronic structure and interfacial carrier dynamics in relevant systems, there is a real need to develop and utilize new methods to study the surface electronic structure of these materials in real time with chemical state resolution.

1.2 Time-Resolved Optical Methods

A number of optical spectroscopies exist for measuring time-resolved dynamics, including pump-probe transient absorption,[50–53] transient reflection,[54–56] and transient grating spectroscopy[57,58] photoluminescence[59,60] and time correlated single photon counting,[61,62] two photon photoemission,[63–65] and a number of multidimensional[66–68] and nonlinear techniques.[69,70] Many papers have been devoted to describing the utility of these methods.

A challenge of optical spectroscopy in the ultraviolet (UV), visible (VIS), and near infrared (NIR) spectral ranges is the difficulty associated with interpreting broad, overlapping features in terms of the chemical states involved in these transitions.[71] The valence and conduction band states involved in optically driven transitions straddle the Fermi level and are the only energy levels that can be accessed by the approximately 1–6 eV photon energies associated with UV/VIS/NIR spectroscopy. These bands are composed of the hybridized energy levels resulting from atomic bonding and anti-bonding interactions in extended crystals.[72,73] Because these interactions give rise to a solid-state band structure where atomic orbitals are significantly broadened via extended bonding interactions, transitions probed by optical absorption are correspondingly broad and often overlap. As a result, it is not trivial to assign absorption features to specific transitions in a solid due to the delocalized nature of these hybridized states and the large extent of overlap between the various features.

This challenge is depicted for the case of α-Fe_2O_3 in Figure 1, where the optical absorption spectrum shows seven broad, overlapping features between 2 and 5.5 eV. However, the chemical origin of these transitions remains a question of significant interest,[71,74,75] where possibilities include 1) intraband d-d excitations associated with a Mott-Hubbard band gap, 2) interband excitations associated with a charge transfer band gap, and 3) absorption by mid-gap states resulting from electronic and structural defects. Because of intense interest in the use of metal oxide semiconductors as photocatalysts, many time-resolved studies based on optical transient absorption have been performed to understand the relationship between photoinduced charge carrier dynamics and the resulting photocatalytic activity. Based on these studies, spectral signatures of carrier trapping at defect states have been assigned.[76–79] However, using only UV/VIS/NIR absorption the chemical origin of the implicated trap states (i.e. oxygen vacancy, metal vacancy, small polaron, etc.) is often not discernable.

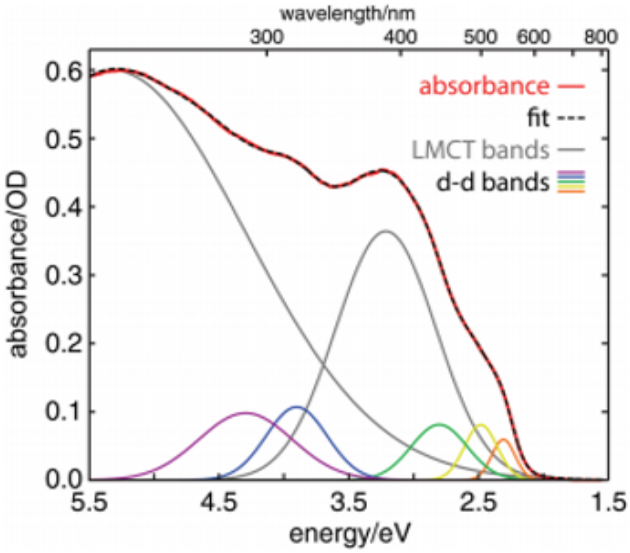

Fig. 1 The reflectance-corrected steady-state optical absorption spectrum of a 20 nm hematite thin film (red). The spectrum was fit (dashed black) to the sum of seven Gaussian bands, which are plotted individually. Reprinted with permission from ref.71. Copyright 2016 Royal Society of Chemistry.

1.3 Time-Resolved X-Ray and XUV Absorption

In contrast to valence band excitations measured by UV/VIS/NIR absorption, extreme ultraviolet (XUV) and X-ray absorption spectroscopies probe core-to-valence transitions.[74,80] To a first approximation, atomic core levels do not participate in chemical bonding, so they are not appreciably broadened or shifted in a solid material relative to isolated atoms. This means that in solid-state spectroscopy, the core-hole energy can act as an element specific tag where the measured transition energy reflects the atomic core-level involved and includes shifts due to final state effects while the near edge fine structure provides detailed information about the valence band electronic structure with element specific resolution.[81] Figure 2 schematically depicts this comparison between UV/VIS/NIR spectroscopy of valence states and core-hole spectroscopy accessible only in the XUV and X-ray spectral regions. Part A shows a comparison between the element-specific transitions measured by a broad band XUV pulse and the optical absorption spectrum measured by a UV/VIS/NIR probe pulse. Part B depicts how the broad band XUV pulse can be used to follow valance band electron dynamics with element specific resolution in an optical pump, XUV probe experiment.

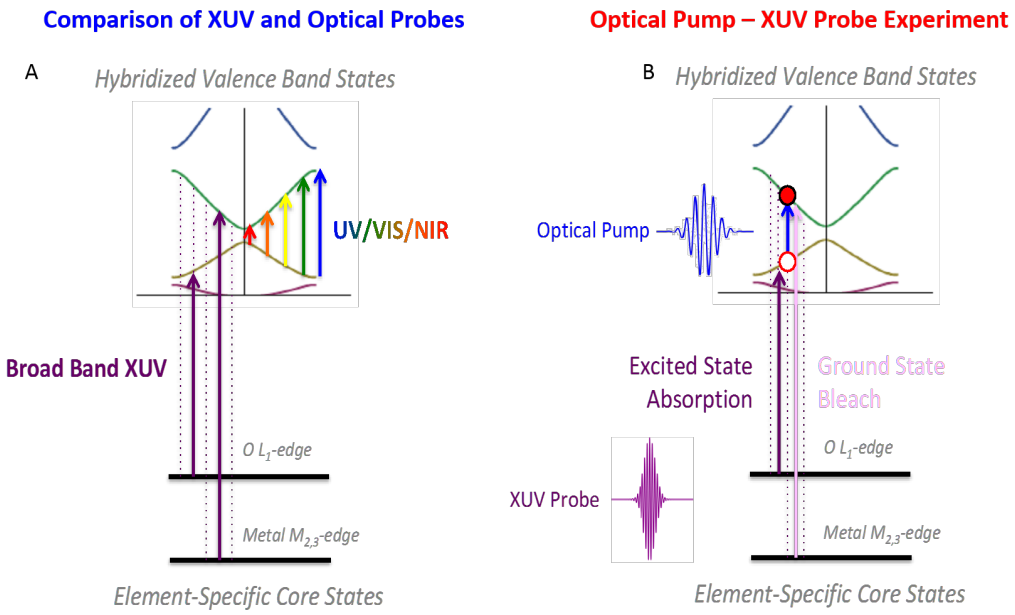

Fig. 2 (A) Valence band transitions as probed by UV/VIS/NIR absorption lead to spectra with many overlapping features due to strong valence orbital hybridization. Core-to-valence transitions as probed by broad band XUV absorption provide element-specific electronic structure information. (B) In an optical pump, XUV probe experiment the pump initiates valence band excitation which is subsequently probed by the element specific broad band XUV beam. As a result, detailed understanding of the valence band electronic structure is achieved with ultrafast time resolution and chemical state specificity.

For this reason X-ray absorption spectroscopy can provide detailed information, not only on the elemental composition of a material, but also on the oxidation states, spin states, and ligand coordination geometry, making these methods particularly powerful for detailed electronic structure characterization.[82] Furthermore, the theory of X-ray absorption is well developed, and computational methods exist for interpreting X-ray spectra, where absorption edge onset, near edge multiplet structure, and extended edge fine structure yield detailed information on both the electronic and crystalline structure of a material.[81,83,84] Despite the attractive benefits of XUV and X-ray absorption spectroscopy, the development of X-ray light sources with the ability to resolve ultrafast electron dynamics has, until recently, limited progress in this field.

1.4 Ultrafast X-Ray and XUV Light Sources

Perhaps the most developed and utilized source for transient X-ray absorption spectroscopy is third generation synchrotron facilities which produce pulses of 30–100 ps duration as determined by the equilibrium length of the electron bunch. Most transient x-ray absorption experiments at these facilities report a time resolution on the order of 80 ps.[71,85–87]

Extended efforts to develop X-ray light sources with ultrafast pulse durations and high peak and average power have resulted in the recent availability of X-ray free electron lasers (XFELs).[88–92] These fourth generation light sources produce fs pulses of coherent X-ray radiation with a fluence that far exceeds that of a third generation synchrotron. Several XFELs currently exist that offer the capability to perform ultrafast transient X-ray absorption.[89–91]

Tabletop generation of X-ray radiation based on a laser driven processes offers an attractive alternative to X-ray absorption spectroscopy at large-scale facilities. X-ray lines produced by laser plasma generation from a solid or liquid target have been used primarily for transient x-ray diffraction rather than x-ray absorption.[93–95] Pulses produced by this technique are on the order of 100s of fs.[96–98]

High harmonic generation (HHG) from a fs driving laser can produce ultrafast pulses in XUV and soft X-ray spectral regions. Pulse durations accessible by HHG range from 100 fs to <100 as.[99–102] Using an 800 nm driving field, the HHG can produce XUV light with photon energies up to approximately 150 eV. It has been recently demonstrated that using a mid IR driving field, this energy range can be extended to the soft X-ray range beyond the carbon K-edge at 285 eV.[103–105]

Returning to the question of optical absorption bands in Fe_2O_3 as an example, Vura-Weis et al. showed that photoexcitation at 400 nm excites a charge transfer band gap transition, which is analogous to a ligand-to-metal charge transfer transition in a molecular complex, where an electron is moved from O 2p valence band states to Fe 3d conduction band states.[74]

This ability of XUV transient absorption spectroscopy to follow ultrafast processes with chemical state resolution opens many exciting opportunities with respect to detailed studies of electron dynamics in energy conversion materials. Leone and co-workers have extended these studies to a range of additional semiconductors demonstrating time resolution ranging from 100 fs to the as regime.[106–110] Here we describe extending ultrafast XUV absorption spectroscopy to follow electron dynamics with chemical state resolution and surface sensitivity.

1.5 XUV Reflection-Absorption Spectroscopy of Surfaces

Treating surface and interfacial electron dynamics as a special case of condensed phase electron dynamics, there has not been extensive focus on surface electron dynamics as measured by X-ray absorption spectroscopy. This is partly because most surface sensitive spectroscopy is based on photoemission rather than absorption spectroscopy, where the surface sensitivity is determined by the inelastic mean free path or escape depth of a photoelectron. [111] Several types of time-resolved photoemission studies exist, including two photon photoemission (2PPE) [112,113] and optical pump, XUV probe photoemission spectroscopy. [114,115] We note that 2PPE exclusively measures valence band electron dynamics as the photon energies employed are not sufficiently high to ionize electrons from core orbitals. XUV light produced by HHG can ionize core electrons, and there have been several recent studies demonstrating the ability to probe photoemission from element specific core states using time-resolved XUV photoemission with a HHG light source. [36,116]

Building on the capabilities of time-resolved photoemission studies, there are several advantages of X-ray absorption spectroscopy, which motivate the development of surface sensitive X-ray absorption described here. Photoemission spectroscopy measures the kinetic energy of electrons ejected into vacuum providing information only on the core electron binding energy. In X-ray absorption measurements the absolute core-hole transition energy serves as an element specific tag similar to X-ray photoelectron spectroscopy, while the absorption lineshape can be interpreted as a projection of valence band electronic structure. For this reason X-ray absorption spectroscopy has been widely used to measure local coordination and electronic structure with element-specific resolution in a variety of molecular systems. [117–120] This article focuses on our recent efforts to extend these measurements to the study of ultrafast electron dynamics at surfaces.

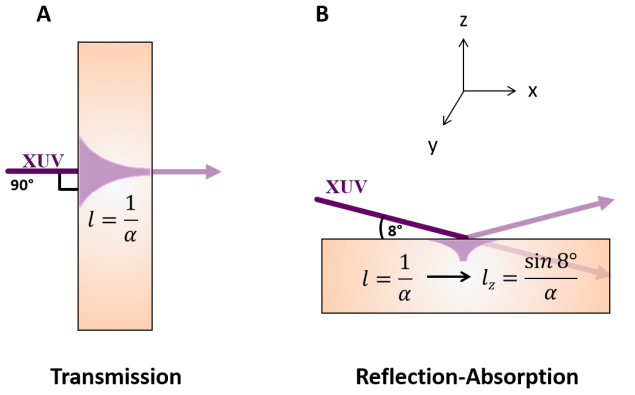

Fig. 3 12

To achieve surface sensitivity during transient XUV absorption measurements, we have adopted a reflection-absorption (RA) geometry, where the XUV probe beam reflects from a sample surface at a near grazing incidence angle. [121–123] A schematic of this reflection experiment compared to an absorption experiment in transmission geometry is depicted in Figure 3. In a transmission geometry, the sampling depth can be approximated as the inverse of the attenuation coefficient as shown in panel A. Considering this same interaction length now projected at a near grazing incidence, the probe depth relative to the sample normal can be given as

$$l_z = \frac{\sin\theta}{\alpha} \quad (1)$$

where l_z is the attenuation length in the direction normal to the sample surface, α is the attenuation coefficient of the XUV probe beam, and θ is the incidence angle of the probe beam relative to the sample plane as shown in panel B. As described below, measuring the resonant attenuation of the specular reflection provides analogous information to a transmission mode XUV absorption experiment. However, given the high resonant attenuation coefficients for metal oxides shown in Table 1, the interaction of the probe beam in this reflection measurement only extends several nm from the sample surface, making XUV-RA spectroscopy selective to a material surface.

Table 1 Attenuation coefficients and probe beam interaction regions in transmission and reflection-absorption experiments for Fe_2O_3, Co_3O_4, and NiO.

Metal oxide	α / nm^{-1}	l_z / nm
Fe_2O_3	0.102 [74]	1.36
Co_3O_4	0.036 [106]	3.87
NiO	0.064 [124]	2.17
TiO_2	0.136 [124]	1.02

In addition to surface sensitivity, XUV-RA spectroscopy is compatible with the study of functional materials. Due to the short transmission length of XUV radiation, absorption spectroscopy is typically limited to samples with thickness of approximately 100 nm deposited to XUV transmissive substrates. [74] In contrast, XUV-RA measurements can be performed on materials of any thickness, regardless of substrate. This is especially important in the study of catalytic materials where altering the thickness or underlying substrate of a catalyst can significantly influence its catalytic performance.

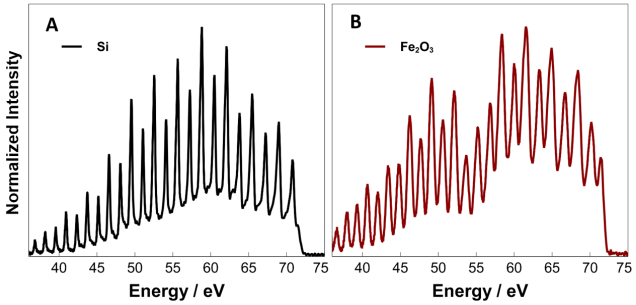

Fig. 4 XUV harmonic spectrum generated in Ne gas as measured after reflectance from a Si mirror (A) and from a Fe_2O_3 sample (B). The dip at approximately 55 eV in spectrum B reflects resonant attenuation by the Fe $M_{2,3}$-edge absorption. The generation of both even and odd order harmonics is achieved by mixing the 800 nm driving field with a 400 nm symmetry breaking field to achieve a continuous, broad band spectrum. Adapted with permission from ref.121. Copyright 2017 American Chemical Society.

2 Developing XUV Reflection-Absorption Spectroscopy

2.1 Instrument Description and Methods

Figure 4 shows the spectral profile produced by HHG in neon gas using an 800 nm driving field (pulse energy: 2.0 mJ, pulse duration: 35 fs). No even order harmonics can be generated in a centrosymmetric medium. To produce an XUV probe spectrum containing both even and odd harmonics, a 400 nm symmetry breaking field (pulse energy: 45 μJ) is overlapped with the 800 nm driving field in the gas interaction region. This allows for a more continuous spectrum to use as an XUV analog to white light. Despite the frequency comb present in this spectrum, even the valley regions have sufficient intensity for measuring XUV absorption across the entire spectral window shown. As will be described in detail below, this XUV region accessible by HHG is ideal for core-level spectroscopy at the $M_{2,3}$-edges of the 3d transition metals.

Details of the experimental procedure for XUV-RA spectroscopy have been described elsewhere.[121] In short, the XUV beam is focused onto the sample at an incident angle of 8° relative to the sample plane using a toroidal mirror. The XUV beam reflected from the sample is then spectrally dispersed onto a CCD detector using a spherical grating. A diagram of the instrument is given in Figure 5. For ground state measurements, the reflectance of a sample (R_{sample}) is measured with respect to a Si reference as given by

$$R_{sample} = \frac{I_{sample}}{I_{Si}} \tag{2}$$

where I_{sample} and I_{Si} are the reflected XUV flux from the sample of interest and the Si reference, respectively. To put this measured spectrum in log units and correct for the known reflectance of Si, Reflection-Absorption is calculated as

$$RA = -log(R_{sample} \cdot R_{Si}) \tag{3}$$

Reflected XUV harmonics from Si and Fe_2O_3 are shown in Figure 4A and 4B, respectively. For time-resolved measurements, the XUV flux reflected from the sample is measured with the optical pump beam both on and off as a function of time delay between pump and probe pulses. The transient RA signal is reported in units of ΔmOD as given by

$$\Delta mOD = -log\left(\frac{I_{pump\ on}}{I_{pump\ off}}\right) \cdot 10^3 \tag{4}$$

2.2 Interpreting XUV Reflection-Absorption Spectra

As shown in Figure 6 XUV-RA spectra differ significantly from those measured in a transmission experiment of the same material. Therefore, it is pivotal to understand the origin of the difference in XUV-RA lineshapes compared to the traditional transmission experiments in order to obtain the same chemically rich information available in a traditional absorption experiment.

To address this issue, we have adapted a semi-empirical method to simulate an XUV-RA spectra from its known transmission analogue. This simulation method reveals the physical origin of the distinct lineshapes measured by XUV-RA spectroscopy. The simulation procedure includes a semi-empirical charge transfer multiplet theory developed by de Groot[125] and classical electromagnetic theory developed by Fresnel.[126] In a transmission experiment, the spectrum is dominated by the imaginary part of the refractive index (k), a descriptor for the absorptive loss of radiation. In contrast, reflection measurements probe the real part of the refractive index (n) – responsible for the reflection, non-resonant transmission, and the dispersion of light in a material – along with k. The following summarizes the steps to simulate XUV-RA spectra. The absorption cross-section as a function of XUV wavelength is first obtained from a ligand field multiplet calculation developed by de Groot and co-workers.[125] The absorption cross section (σ) of a material is directly related to k as given in Equation 5

$$k = \frac{\lambda \eta \sigma}{4\pi} \tag{5}$$

Here, λ is the wavelength of incident light and η is the number density of the resonant absorber. The real part of the refractive index is obtained by numerical integration using Kramers-Kronig relation.

$$n(\omega) = 1 + \frac{2}{\pi} P \int_0^\infty \frac{\omega' k(\omega')}{\omega'^2 - \omega^2} d\omega' \tag{6}$$

In Equation 6, P refers to the Cauchy principle value of the integral, ω is the angular frequency of light, and ω' is the angular frequency of light over which the integration is performed (i.e., the domain of the calculation). The complex refractive index, $N = n + i \cdot k$, is then calculated from the derived k and n.

Having obtained the complex refractive index, the XUV-RA spectrum is obtained from the following equation

$$RA = -log_{10}|r|^2 \tag{7}$$

where r is the classical Fresnel factor for the reflectance (r) of p-polarized light, corrected by the Debye-Waller factor as given by

$$r = \frac{-N^2 cos(\theta) + \sqrt{N^2 - sin^2(\theta)}}{N^2 cos(\theta) + \sqrt{N^2 - sin^2(\theta)}} \cdot exp\left(\frac{-16\pi^2 R_q^2 cos^2(\theta)}{3\lambda^2}\right) \tag{8}$$

where θ is the angle of incidence relative to the surface normal ($\theta = 82°$), λ is the wavelength of light, R_q is the root-mean-square surface roughness, and r is a complex number due to N. In the experiments described below, we have used atomic force microscopy (AFM) to directly measure R_q, so this parameter is not adjustable in the spectral simulation.

In related work Berlasso and co-workers measured reflectance spectra at the Fe and Co $M_{2,3}$-edges and used these measured spectra to obtain the imaginary part of the refractive index via a Kramers-Kronig transformation.[127] However, these studies were only applied to atomically smooth, single crystal samples so questions related to the effects of surface morphology on the measured XUV-RA spectra were not addressed. As shown below, sample

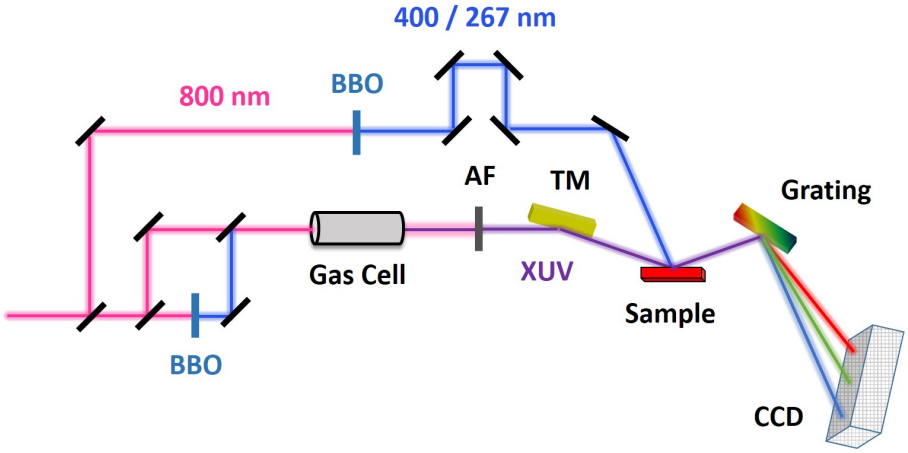

Fig. 5 Overview of the XUV reflection-absorption spectrometer. High harmonic generation (HHG) occurs in a gas cell by a two color driving field. Once generated, the residual 800 and 400 nm beams are removed by an Al filter (AF) which only transmits the XUV flux up to the 72 eV Al absorption edge. The XUV beam is focused onto the sample by a toroidal mirror (TM) and spectrally dispersed onto a CCD camera by a spherical grating. Prior to HHG a portion of the 800 nm fundamental is separated for use as an optical pump pulse. This beam is frequency doubled (tripled) using β-barium borate (BBO) crystals to generate a 400 (267) nm pump beam with a variable time delay.

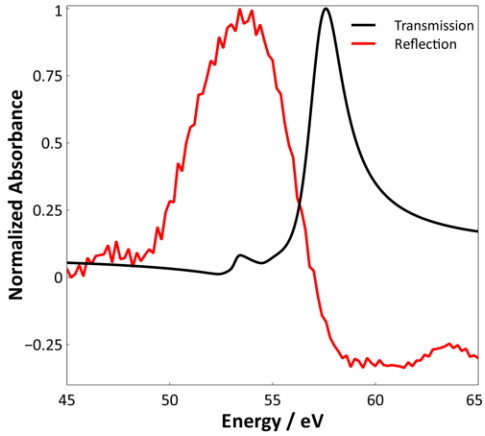

Fig. 6 Normalized static spectrum of Fe_2O_3 as measured by Reflection-Absorption (red) and transmission (black) experiments. Adapted with permission from ref.121. Copyright 2017 American Chemical Society.

morphology has a strong influence on the measured XUV-RA lineshapes, and these effects must be quantitatively accounted for to extract the oxidation state, spin state, and crystal field information available from the near edge fine structure in a transmission measurement.

To address this issue we have measured the XUV-RA spectra of single-crystalline (SC) Fe_2O_3, polycrystalline (PC) Fe_2O_3 and PC $CuFeO_2$. In all three materials, the high spin Fe^{3+} center is octahedrally coordinated by O^{2-} ligand, however, these materials each have a distinct surface roughness. Consequently, their XUV-RA spectra as shown in Figure 7 are significantly different from one another as anticipated. To account for these changes in the XUV-RA lineshape, we have used a modified form of the classical Fresnel equation, which includes the exponential term given in equation 8, known as the Debye-Waller factor. The Debye-Waller factor accounts for the fact that the non-resonant surface scattering increases with decreasing the wavelength of the XUV light and with increasing the surface roughness.[127] As a result, this simulation model quantitatively considers the effect of non-resonance surface scattering due to changes in the surface morphology in the measured XUV-RA lineshapes.

In addition to inclusion of the Debye-Waller factor, the simulation requires a wavelength independent vertical offset in the real part of the refractive index in order to reproduce the experimental spectra. Additionally, we find that the magnitude of this correction depends strongly on the surface morphology of the sample. For the three materials containing nearly identical Fe^{3+} metal centers shown in Figure 7, surface roughness increases from SC Fe_2O_3 ($R_q < 0.2$ nm), to PC Fe_2O_3 ($R_q = 10$ nm), to PC $CuFeO_2$ ($R_q = 27$ nm).

In simulating these spectra, we find that an increasingly negative vertical offset of n is required to reproduce the experimental spectra. In absolute units these offsets in n are -0.0100 (SC Fe_2O_3), -0.0140 (PC Fe_2O_3), and -0.0155 ($CuFeO_2$). Applying these offsets, the resulting simulated XUV-RA spectra (black traces) provide excellent agreement with the experimental spectra (red traces) as shown in Figure 7. We believe that this offset reflects morphology-induced changes in the non-resonant photoemission background of the samples. To explain why the magnitude of the vertical offset in n correlates with surface roughness, it is known that the intensity of non-resonant photoemission is strongly influenced by surface morphology.[128–130] In this way the simulation model accounts for changes in the XUV-RA lineshapes due to this morphology-dependent photoemission baseline. Using this developed simulation procedure we can accurately simulate the ground state XUV-RA spectra of TiO_2, Cr_2O_3, Fe_2O_3, NiO as shown in Figure 8.

The spectral simulations show excellent agreement with the measured XUV spectra. We note that the lineshape and XUV $M_{2,3}$-edge absorption position are different in each of the metal oxides studied.

As shown, the resonance position of the $M_{2,3}$-edge transitions (3p

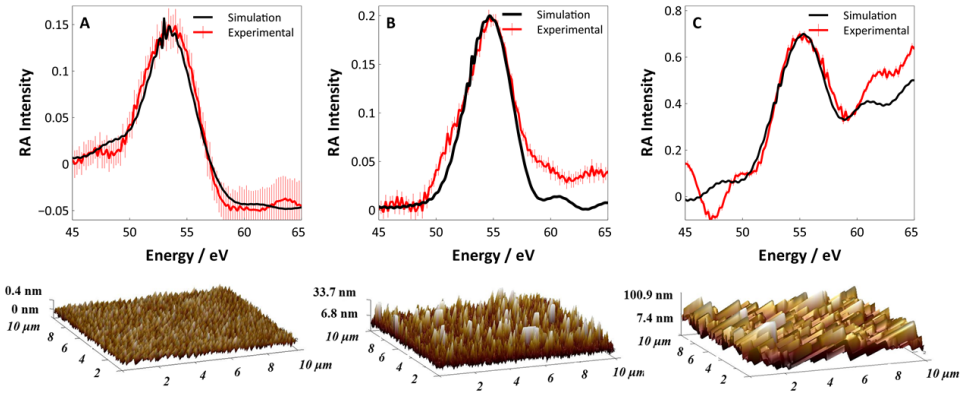

Fig. 7 Simulated (black) and experimental (red) RA spectra for (A) SC Fe_2O_3, (B) PC Fe_2O_3, and (C) $CuFeO_2$. All RA simulations differ only by adjusting a wavelength-independent offset in the real part of the refractive index to take into account the relative surface morphology. Below each spectrum is a representative AFM image of the surface roughness for each material (SC Fe_2O_3, $R_q < 0.2$ nm; PC Fe_2O_3, R_q = 10 nm; $CuFeO_2$, $R_q \approx$ 27 nm). The error bars on the experimental spectra are the standard deviation associated with each data point. Adapted with permission from ref.121. Copyright 2017 American Chemical Society.

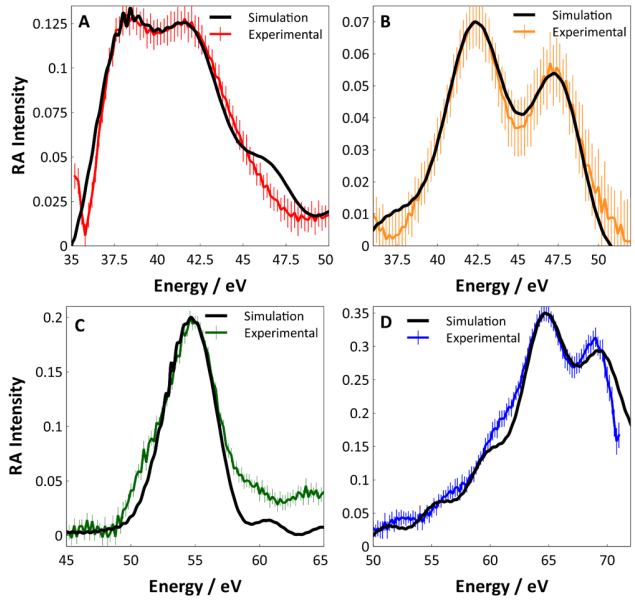

Fig. 8 Simulated (black) and experimental (color) static XUV-RA spectra of (A) TiO_2, (B) Cr_2O_3, (C) PC Fe_2O_3 and (D) NiO. The error bars on the experimental spectra are the standard deviation associated with each data point. Adapted with permission from ref.121. Copyright 2017 American Chemical Society.

$\rightarrow$ 3d) increases with atomic number. This is because the binding energy of the 3p orbital scales with effective nuclear charge from left to the right across the periodic table. In contrast to the 3p core orbitals, the binding energy of 3d valence orbitals is less influenced by nuclear charge due to screening by core electrons. As a result, the 3p $\rightarrow$ 3d transition energy increases with atomic number along the series TiO_2, Cr_2O_3, Fe_2O_3, and NiO, giving rise to the element specificity of core-hole spectroscopy, which is preserved in the XUV-RA measurements shown here.

2.3 Experimental Validation of Surface Sensitivity

As described above, the probe depth of a near grazing angle XUV-RA measurement is expected to be on the order of one to several nm. To experimentally validate this prediction, XUV-RA spectra have been collected for TiO_2 thin films of variable thickness (3 nm, 4 nm, 6 nm, 8 nm, 25 nm) grown by atomic layer deposition (ALD) on an SiO_2 substrate. To determine the probe depth of the measurement, the resonant intensity at the Ti $M_{2,3}$-edge has been plotted as a function of the TiO_2 film thickness (see purple squares in Figure 9). The XUV-RA intensity at the Ti $M_{2,3}$-edge increases with TiO_2 film thickness as long as the thickness is less than the probe depth of the measurement. However, when the film thickness exceeds the measured probe depth, no further signal enhancement is observed.

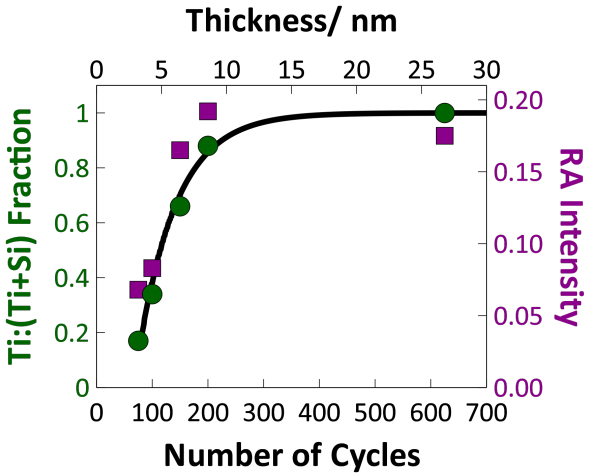

Fig. 9 The experimentally determined probe depth for XUV-RA spectroscopy and XPS. Fitting an exponential rise to the XPS data points yields a probe depth of 2.8 nm (shown by the black line). Adapted with permission from ref.121. Copyright 2017 American Chemical Society.

XPS measurements have also been collected for each sample. From XPS it is possible to determine the atomic fraction of Ti and Si by taking a ratio of the Ti 3d and the Si 2p XPS lines and

correcting for the atomic sensitivity factors. Plotting this fraction as a function of film thickness and fitting to an exponential rise reveals the probe depth of this XPS measurement, where the Ti atomic fraction approaches 100% as the TiO_2 film thickness exceeds the XPS probe depth. This probe depth is found to be 2.8 nm as shown by the best fit to the green circles in Figure 9. This value closely matches the known surface sensitivity for XPS based on tabulated values for the inelastic mean free path of the Ti 3p and Si 2p photoelectrons. Comparing the XUV-RA intensity with the Ti atomic fraction determined by XPS shows that the XUV-RA probe depth for these samples is similar within error to the probe depth of XPS which is considered one of the primary tools for surface sensitive electronic structure characterization. The measured probe depth is slightly deeper than what is predicted in Table 1 which assumes a perfect planar surface. This result confirms that XUV-RA measurements are likewise selective to surface electronic structure, providing an experimental platform for studying ultrafast surface dynamics with chemical state resolution.

3 Surface Electron Dynamics Probed by XUV Reflection-Absorption Spectroscopy

3.1 Correlations Between Surface Electron Trapping and Small Polaron Formation in Fe_2O_3

Fe_2O_3 is a widely studied photocatalyst for water splitting. Its valence band edge is ideally positioned to drive water oxidation, and its direct band gap of 2.2 eV makes it a strong absorber of visible light. Despite these advantages, its actual efficiency even in best cases is less than half of predicted limits.[131,132] This is believed to be a result of surface electron trapping and small polaron formation, which severely limit carrier mobility and lifetimes.[77,133,134] As described below, recent measurements of surface carrier dynamics in Fe_2O_3 photoexcited at 400 nm using XUV-RA spectroscopy are able to detect spectral signatures of surface electron trapping and small polaron formation, which both occur on the sub-ps time scale.[122] Interestingly, we find no difference in the trapping rate as a function of surface morphology or grain size suggesting that charge trapping in this material is not mediated by structural defects. Rather we hypothesize that lattice expansion associated with small polaron formation may be the driving force for ultrafast localization of electron density to the Fe_2O_3 surface.

Figure 10 shows transient XUV-RA contour plots of SC Fe_2O_3 (panel A) and PC Fe_2O_3 (panel B) for pump probe time delays between 0 and 5 ps. Despite having different ground state spectra (see Figure 7), the transient spectra are nearly identical for SC and PC hematite. Immediately following photoexcitation by 400 nm light, a ground state bleach centered at 54 eV is present in both materials. After 660 fs this initial bleach evolves into a final excited state with a positive feature at 52 eV and a blue shifted bleach at 55.4 eV. The spectral evolution from the initial bleach-only excited state to the final excited state is nearly identical in both SC and PC hematite samples. Once the final excited state is formed, minimal spectral evolution is observed for time delays up to 350 ps.

A two-step sequential kinetic model can describe the measured kinetics for both SC and PC Fe_2O_3. The resulting initial and final state spectra are shown in Figure 11A and B. Due to the close similarity of SC and PC samples, results are only shown for PC Fe_2O_3 here, and analogous plots for SC Fe_2O_3 have been reported previously.[122] The time constant for spectral evolution between initial an final states was also determined by global fitting to be 640 ± 20 fs for PC Fe_2O_3 and 680 ± 30 fs for SC Fe_2O_3.

To accurately assign the states which give rise to these transient spectra, it is necessary to consider the real (k) and imaginary (n) components of the complex refractive index. Panel C of Figure 11 shows the real (upper gray curve) and imaginary (lower black curve) parts of the complex refractive index for ground state of Fe_2O_3. Transmission measurements, which probe only the imaginary part (k), have shown that excitation produces an initial transient spectrum that can be simulated as a one-electron reduction of Fe^{3+} to Fe^{2+}.[74] The imaginary refractive index associated with this Fe^{2+} excited state is also shown in Figure 11C (lower red curve). In other words, the evolution from black to red curves in the imaginary component of the complex refractive index describes the measured bulk transient spectrum. Using the method described above to compute an XUV-RA spectrum from the complex refractive index, the initial transient state can be simulated as the difference between Fe^{2+} excited and Fe^{3+} ground states shown here. The black curve in panel A of Figure 11 shows the results of this simulation, while the blue curve shows the experimentally measured initial state spectrum. Note that in this simulation, we have assumed no evolution of the real part of the refractive index immediately following photoexcitation. This assumption provides a good match to the initial transient spectrum.

Even though the real and imaginary parts of the refractive index are mathematically related by Kramers-Kronig relations, the idea that they can evolve on separate time scales can be understood by considering that their respective probe depths are different. Specifically, the induced polarization at the surface undergoes absorptive damping for a resonant material. This damping occurs in the entire volume of the induced polarization and is reflected only in the imaginary part of the complex refractive index. This means that even though n and k are sensitive to a material interface, k alone probes the sub-surface for a given spatial distribution of the induced polarization.

Parts B and D in Figure 11 show the effect of subsequent evolution of the real part of the refractive index following photoexcitation. Panel D shows the real and imaginary components of the complex refractive index for the Fe^{2+} excited state. Dashed lines show the case for an unshifted Fe^{2+} excited state, while the solid lines show the effect of spectral blue shifting due to fast expansion of the oxide lattice. The simulated transient spectra are shown in panel B for a static and expanded lattice. Both simulated spectra qualitatively match the final measured transient state shown in red. From this we see that the rise of positive transient absorption, which is notably absent in the initial excited state, can be described as the time-dependent evolution of the real part of the complex refractive index. Comparing the peak positions in the two simulated spectra to the experimental spectrum, it is clear lattice expansion has occurred. Consequently, we assign this shift as the spectral signature of carrier self-trapping by small polaron

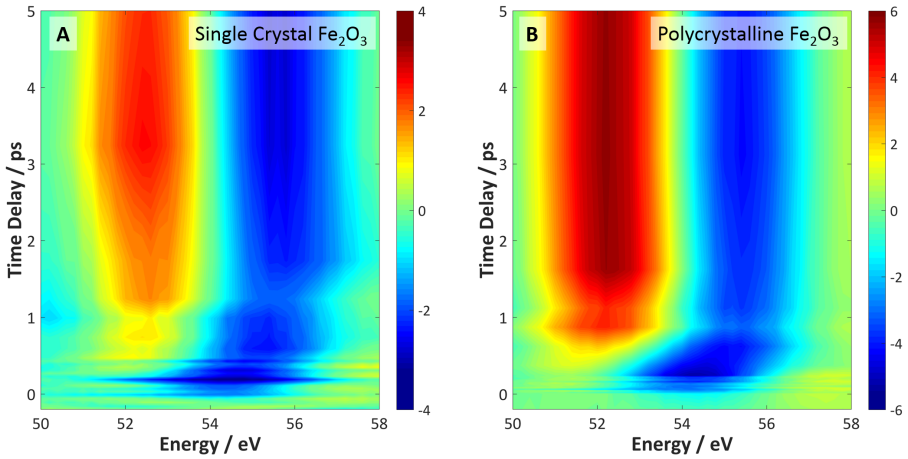

Fig. 10 Experimental contour plots for SC (A) and PC (B) Fe_2O_3 depicting the spectral evolution up to 5 ps post-excitation. Adapted with permission from ref.122. Copyright 2017 Royal Society of Chemistry.

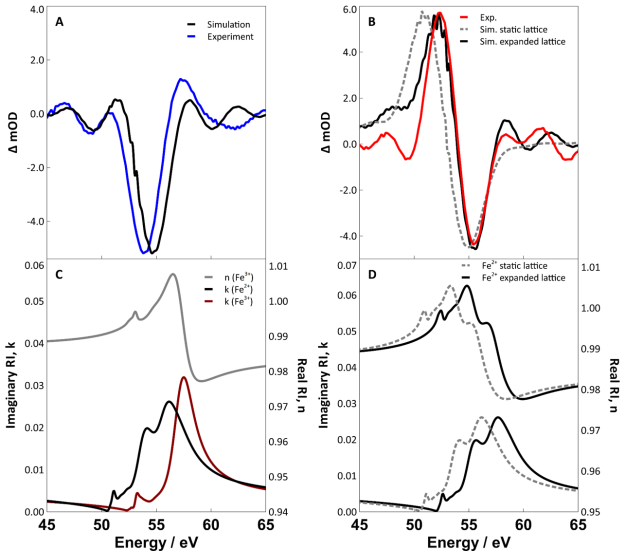

Fig. 11 (A) Experimental (blue) and simulated difference spectrum (black) of the initial excited state which corresponds to an RA spectrum where n has yet to respond to the formation of the charge transfer state. (B) Difference spectra resulting from expanded (black) and static (dashed gray) real and imaginary parts of the refractive index for Fe^{2+}. (C) Real part of the refractive index of Fe^{3+} (gray) and imaginary parts of the refractive index of Fe^{3+} (dark red) and Fe^{2+} (black). (D) Real and imaginary parts of the refractive index for Fe^{2+} with (black) and without (dashed gray) lattice expansion. Adapted with permission from ref.122. Copyright 2017 Royal Society of Chemistry.

formation.

These observations are in general agreement with recent measurements of wavelength dependent polaron dynamics in Fe_2O_3 using XUV transient absorption spectroscopy.[110] In both reflection and transmission measurements, an initial charge transfer excitation is observed as electron density is shifted from the O 2p valence band to the Fe 3d conduction band. This charge transfer state subsequently forms a trapped polaron, which is indicated by a $>$ 1 eV blue shift in the transient spectrum, and this shift is clearly visible in both transmission and reflection measurements. Two reasons for this shift have been proposed: First is the decrease in Fe-O bond covalency following expansion of the oxide lattice, which is known to increase the core-hole transition energy.[135] The second is splitting of the 3p core states involved in the $M_{2,3}$-edge absorption as has been predicted theoretically.[136]

Despite these similarities, several differences exist between XUV transmission measurements and reflection measurements of the same system. First, the initial state in a transmission experiment shows both a ground state bleach and an excited state absorption. In contrast, the transient RA spectrum of the initial state shows only a ground state bleach. As explained above, spectral simulation shows that this observation can be understood as the fast response of the imaginary or absorptive component of the refractive index, which samples the material sub-surface to a depth of several nm, followed by a delayed response of the real or dispersive part of the refractive index, which samples only the surface. Consequently, the rise of excited state absorption in the XUV-RA experiment reflects the localization of electron density contained in the newly populated Fe 3d conduction band to the material surface. This surface localization of charge density induces a response in the real part of the refractive index on the time scale of surface electron trapping. As reported, this trapping process occurs with a time constant of approximately 660 fs for both SC and PC Fe_2O_3. Nearly identical kinetics measured for both SC and PC Fe_2O_3 confirm that surface and grain boundary defect states do not mediate surface electron trapping observed here.

Second, we observe that the spectral signatures of polaron formation (blue shift) and surface electron trapping (positive excited state absorption) evolve with a single correlated time constant. This time constant of 660 fs is notably slower than polaron formation rates measured in bulk via XUV transmission experiments. Kinetic analysis has been performed based on transmission measurements, which accounts for electron-phonon scattering rates and bimolecular decay of electrons and phonons to form polarons.[110] Although similar kinetic analysis has not been performed using data obtained from reflection measurements, the

overall time constant for spectral evolution in reflection measurements is more than two times slower than transmission measurements (640 ± 20 fs[122] compared to 240 ± 30 fs[74]) when comparing results from a 400 nm pump pulse and identical excitation fractions. The reason for this significant difference is not yet clear. Given the strong dependence of electron-phonon scattering rates on subsequent polaron formation, it will be important to consider these kinetics for the case of surface electron and phonon dynamics, which clearly differ from their bulk analog. The idea of 2-dimensional or surface polarons has been established for a number of thin film systems using 2PPE measurements.[137–139] A common feature of these systems is the unique vibrational modes of a surface or interface relative to the bulk, which mediate carrier self-trapping. An important future direction will be to consider how surface phonon modes[140–142] give rise to unique energetics for carrier self-trapping at surfaces and interfaces, especially in cases where interfacial charge transfer is important for driving surface chemical reactions.

3.2 Valence Band Dynamics and Ultrafast Hole Localization

Ultrafast (∼100 fs to few ps) localization of the photoexcited hole in the valence band of transition metal oxides is important for understanding the photocatalytic water oxidation efficiency.[143–145] The valence band of transition metal oxides has complex electronic structure, primarily composed of M 3d and O 2p states with varying degree of mixing making the detection of hole localization difficult in these materials.[72,75,146] Ground state x-ray absorption spectroscopy (XAS) has been used previously to measure the extent of hybridization between M 3d and O 2p in transition metal oxides.[147,148] However, XAS is indirectly sensitive to the hybridization as it probes the contribution of the O 2p character to the unoccupied M 3d density of states. Previous observations of electron and hole localization by XUV spectroscopy have been reported for thin film of germanium and PbI_2.[109,149] Using time-resolved XUV-RA measurements we are able to directly probe the very fast localization of photogenerated hole in the in the hybridized valence band of transition metal oxides by probing the O L_1-edge [O (2s) → O (2p)] transition.[123] We observe that the hole localizes to O 2p valence band states within the instrument response time (< 100 fs) following photoexcitation. Signature of hole at the O L_1-edge enables the comparison of excited state electronic structure of the hybridized valence band that correlates with water oxidation efficiency in Fe_2O_3, Co_3O_4 and NiO.

Figure 12 compares the transient XUV-RA spectra after 2 ps following photoexcitation for Fe_2O_3, Co_3O_4, NiO and FeS_2. In each case the shaded background represents the static XUV-RA spectra to the corresponding transient. Photoexcited state in Fe_2O_3, $Co_3O_4$and NiO shows a nature of the charge transfer state where photoexcitation [O (2p) → M (3d)] leads to a one electron reduction of the metal center.

This one electron reduction process is generic in each of the metal oxide studied leading to the generation of negative and bathochromically shifted positive features at the metal $M_{2,3}$-edge in the transient absorption spectra as shown in Figure 12A, B and C. The negative feature is associated with the ground state

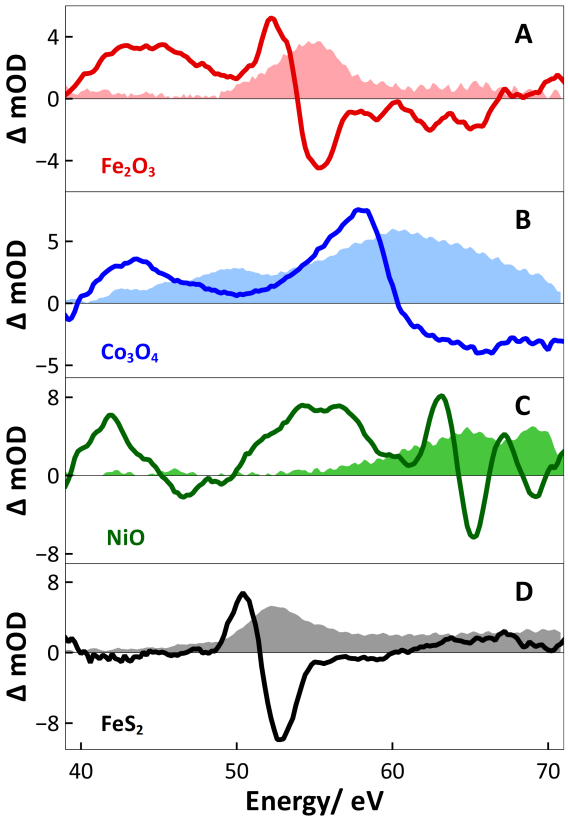

Fig. 12 Transient XUV-RA spectra of (A) Fe_2O_3, (B) Co_3O_4, (C) NiO, and (D) FeS_2 after 2 ps following photoexcitation. Shaded plots represent the corresponding measured static XUV-RA spectra. Adapted with permission from ref.123. Copyright 2018 American Chemical Society.

bleach of the metal center due to the population of photoexcited electrons in the metal 3d conduction band, while the positive feature is associated with the excited state absorption of the reduced metal center. This picture is consistent with the ligand-field multiplet simulations of photoexcited charge transfer state in each metal oxide as has been described in detail previously and confirms our assignment of charge transfer state in photoexcited Fe_2O_3, $Co_3O_4$and NiO.[74,106,121] In addition to the spectral features corresponding to the metal $M_{2,3}$-edge transition, we observe a broad excited state absorption feature around ∼42 eV in Fe_2O_3, Co_3O_4 and NiO as shown in Figure 12 A, B and C, respectively. Surprisingly, according to the Henke table, O L_1-edge (2s → 2p) transition energy (∼41.6 eV) is similar to the common positive absorption feature observed at ∼42 eV in each metal oxide.[124] Consequently, we have assigned this positive feature to an additional absorption channel at the O L_1-edge, where the transition of electrons occurs from O 2s to the hole in the O 2p based valence band following photoexcitation as schematically depicted in Figure 13. To confirm this spectral assignment, we have measured the XUV-RA of photoexcited FeS_2 as shown in Figure 12D. The spectral feature in FeS_2 at the Fe $M_{2,3}$-edge is similar to Fe_2O_3, however, no broad positive feature around ∼42 eV is observed in FeS_2. This confirms our spectral assignment of the broad positive feature at ∼42 eV to the O L_1-edge transition associated with the presence of transient hole in the O 2p based valence band in

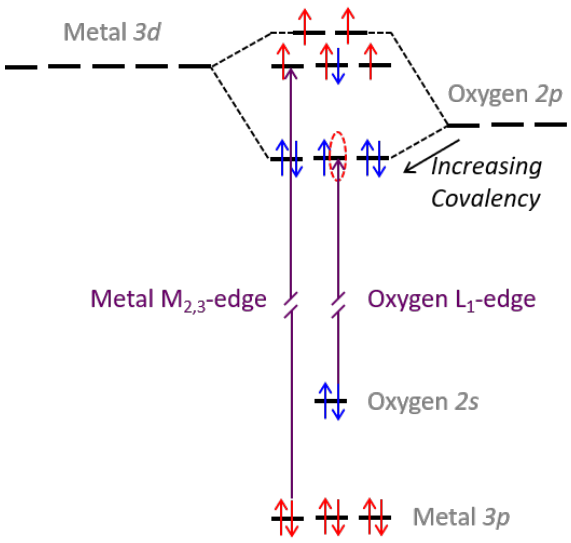

Fig. 13 O L_1-edge absorption is enabled after photoexcitation which removes an electron from the filled 2p shell. Adapted with permission from ref.123. Copyright 2018 American Chemical Society.

photoexcited Fe_2O_3, Co_3O_4 and NiO. The localization of photoexcited hole in the O 2p based valence band additionally validates the nature of charge transfer character of these metal oxide semiconductors.

Careful analysis of the spectral feature at the O L_1-edge in each metal oxides shows that there is a gradual bathochromic shift of the L_1-edge peak position from Fe_2O_3 to Co_3O_4 to NiO. The O L_1-edge transition has been observed at 44 eV, 43 eV, and 42 eV for Fe_2O_3, Co_3O_4, and NiO, respectively. We have attributed this trend to the different degree of hybridization between M 3d and O 2p in the charge transfer photoexcited state of Fe_2O_3, Co_3O_4, and NiO. Figure 13 shows the simplified molecular orbital picture of the M-O bond. This simplified model shows that increasing the effective nuclear charge on the metal center from Fe to Co to Ni leads to increased hybridization between M 3d and O 2p from Fe_2O_3 to Co_3O_4 to NiO. As a result, L_1-edge transition from O 2s core to the hole in the 2p based molecular orbital shows a bathochromic shift from Fe_2O_3 to Co_3O_4 to NiO.

Recent studies on water oxidation reaction involving transition metal oxide catalysts speculate that M-O bond covalency has a dominant impact on the water oxidation kinetics where efficient hybridization between metal 3d and O 2p reinforces the water oxidation efficiency .[135,148,150] The measured overpotential for water oxidation reaction decreases from Fe_2O_3 to Co_3O_4 to NiO.[151] Our observation of increasing M-O bond covalency from Fe_2O_3 to Co_3O_4 to NiO is consistent with the measured trend of water oxidation efficiency, affirming the correlation between covalency and catalytic water oxidation kinetics.

3.3 Measuring the Radii of Highly Localized Charge Transfer Excitons

Poor charge carrier mobility is one of the major reasons of losses experienced during energy conversion in first row transition metal oxide semiconductors.[7,152,153] The charge carrier mobility and catalytic efficiency of these materials are closely related to the interaction between the photoexcited electron-hole and the localization of the exciton.[154] Using pump fluence dependent study of the transient XUV-RA intensity, we find that the photoexcited electrons and holes are separated by approximately one M-O bond length in Fe_2O_3, Co_3O_4 and NiO.[123]

The measured transient XUV-RA intensity shows a behavior of signal saturation at higher pump fluence in each of the metal oxides studied. This is primarily due to the exciton-exciton annihilation process as a result of increased exciton density.[155,156] Exciton-exciton annihilation occurs via non-radiative Auger recombination mechanism. In this process, a bimolecular interaction between two excitons leads to a rapid electron-hole recombination of one exciton, while the released energy is used to promote the other exciton to a doubly excited state. The lifetime of the doubly excited exciton is very short and relaxes back to the initial state via electron-phonon scattering.[155,156] The observed saturation behavior of the transient signal has been fitted by the saturable absorber model given by the equation below[157,158]

$$I \propto \frac{\Phi}{\Phi + \Phi_s} \tag{9}$$

where I represents the intensity of the transient signal, Φ is the pump flux and Φ_s is the saturation flux. Assuming the spherical size of the exciton, the fitted Φ_s from the saturable absorber model allows the calculation of the exciton Bohr radius in Fe_2O_3, Co_3O_4 and NiO as given in Table 2.[123]

Table 2 : Summary of the exciton Bohr radius, M-O bond length and lattice constant. Adapted with permission from ref.123. Copyright 2018 American Chemical Society.

	Exciton Bohr radius	M-O bond length	Lattice Constant
Fe_2O_3	2.57 Å	2.05 Å	5.04 Å
Co_3O_4	3.31 Å	1.93 Å	8.07 Å
NiO	4.46 Å	2.08 Å	4.18 Å

We find that the exciton Bohr radii are on the order of one M-O bond length in these metal oxides as shown in Table 2, suggesting a highly localized nature of the exciton. This picture is consistent with the Frenkel exciton model, where excitons tend to be localize within a single unit cell. Gradual increase of the exciton size correlates with the bathochromic shifts of the O L_1-edge peak position from Fe_2O_3, Co_3O_4 to NiO. This observation suggests that excitons prefer to delocalize with increasing M-O bond covalency. Accordingly, these results indicate that the photoexcitation basically occurs across a single M-O bond where hole is localized on O 2p valence band states with electron localized on metal 3d conduction band states.

4 Conclusions and Outlook

The ability to observe surface electron dynamics in real time with chemical state resolution is required to advance the fields of energy conversion and catalysis. This is because performance of these systems is inevitably mediated by charge carrier dynamics at interfaces, which differ significantly from the bulk of the same material due to undercoordination, interface bonding, and

chemical and structural defects. Despite the importance of these processes for numerous applications, much less is currently understood about surface photophysics by comparison to molecular photophysics. This is due largely to the difficulty associated with probing surfaces and interfaces selectively with ultrafast time resolution and chemical state specificity. This challenge highlights the need for the development and utilization of new methods to interrogate surface electronic structure and corresponding dynamics.

In this feature article, we have described recent advances in the development of XUV reflection-absorption spectroscopy. This work is an extension of XUV transient absorption spectroscopy, where core-hole resonances enable the study of element-specific carrier dynamics with fs, or even as, resolution using a tabletop high harmonic light source. XUV spectra collected by reflection from a sample at near grazing angle measure the same resonances. However, this method is surface sensitive having a probe depth of only a few nm. This technique extends the advantage of X-ray absorption, including element, oxidation, and spin state resolution, to the study of surface electron dynamics. Consequently, this method provides complimentary information to other surface techniques such as time resolved photoemission and second order nonlinear spectroscopies.

We have highlighted a number of recent examples showing the utility of XUV reflection-absorption. These include measurement of ultrafast surface electron trapping and small polaron formation in hematite as well as the ability to independently measure electron and hole dynamics by transient spectroscopy at the metal $M_{2,3}$ and O L_1-edges, respectively. Based on these early results, we anticipate that this method will continue to contribute to a detailed understanding of surface electron dynamics in relevant materials, where ultrafast time resolution and chemical state specificity are required to elucidate the mechanisms of charge transfer and energy conversion at surfaces.

5 Conflicts of interest

There are no conflicts of interest to declare.

6 Acknowledgements

Work on design and construction of this instrument and measurement of surface electron dynamics in hematite were supported by the Air Force Office of Scientific Research under AFOSR award number FA9550-15-1-0204. Simulation of XUV-RA spectra, measurement of O L_1-edge spectra, and determination of exciton Bohr radii were supported by the Department of Energy under DOE award number DE-SC0014051. We would also like to thank former and current group members, Dr. Anthony Cirri, Quinn Baker, and Stephen Londo for their contributions to the work described here.

References

1 C. S. Ponseca, P. Chabera, J. Uhlig, P. Persson and V. Sundstrom, *Chem. Rev.*, 2017, **117**, 10940–11024.

2 J. M. Rehm, G. L. McLendon, Y. Nagasawa, K. Yoshihara, J. Moser and M. Grätzel, *J. Chem. Phys.*, 1996, **100**, 9577–9578.

3 P. Narang, R. Sundararaman and H. A. Atwater, *Nanophotonics*, 2016, **5**, 96–111.

4 A. Hagfeldt and M. Grätzel, *Acc. Chem. Res.*, 2000, **33**, 269–277.

5 J. E. Moser, P. Bonnôte and M. Grätzel, *Coord. Chem. Rev.*, 1998, **171**, 245–250.

6 M. A. Fox and M. T. Dulay, *Chem. Rev.*, 1993, **93**, 341–357.

7 A. L. Linsebigler, G. Lu and J. T. Yates Jr, *Chem. Rev.*, 1995, **95**, 735–758.

8 H. Over, *Chem. Rev.*, 2012, **112**, 3356–3426.

9 K.-C. Cheung, W.-L. Wong, D.-L. Ma, T.-S. Lai and K.-Y. Wong, *Coord. Chem. Rev.*, 2007, **251**, 2367–2385.

10 N. J. Cherepy, D. B. Liston, J. A. Lovejoy, H. Deng and J. Z. Zhang, *J. Phys. Chem. B*, 1998, **102**, 770–776.

11 C. Clavero, *Nat. Photonics*, 2014, **8**, 95.

12 C. Ponseca Jr and V. Sundström, *Nanoscale*, 2016, **8**, 6249–6257.

13 Y. Tachibana, J. E. Moser, M. Grätzel, D. R. Klug and J. R. Durrant, *J. Phys. Chem.*, 1996, **100**, 20056–20062.

14 N. A. Anderson and T. Lian, *Annu. Rev. Phys. Chem.*, 2005, **56**, 491–519.

15 A. Chenu and G. D. Scholes, *Annu. Rev. Phys. Chem.*, 2015, **66**, 69–96.

16 I. McConnell, G. Li and G. W. Brudvig, *Chem. Biol.*, 2010, **17**, 434–447.

17 J. Barber, *Chem. Soc. Rev.*, 2009, **38**, 185–196.

18 D. Gust, T. A. Moore and A. L. Moore, *Acc. Chem. Res.*, 2009, **42**, 1890–1898.

19 D. Gust, T. A. Moore and A. L. Moore, *Accounts of Chemical Research*, 2001, **34**, 40–48.

20 S. M. Falke, C. A. Rozzi, D. Brida, M. Maiuri, M. Amato, E. Sommer, A. De Sio, A. Rubio, G. Cerullo, E. Molinari *et al.*, *Science*, 2014, **344**, 1001–1005.

21 J. S. DuChene, B. C. Sweeny, A. C. Johnston-Peck, D. Su, E. A. Stach and W. D. Wei, *Angew. Chem. Int. Ed.*, 2014, **53**, 7887–7891.

22 G. Zhang, G. Kim and W. Choi, *Energy Environ. Sci.*, 2014, **7**, 954–966.

23 M. E.-A. Madjet, A. V. Akimov, F. El-Mellouhi, G. R. Berdiyorov, S. Ashhab, N. Tabet and S. Kais, *Phys. Chem. Chem. Phys.*, 2016, **18**, 5219–5231.

24 W. Cao, Z. Zhang, R. Patterson, Y. Lin, X. Wen, B. P. Veetil, P. Zhang, Q. Zhang, S. Shrestha, G. Conibeer *et al.*, *RSC Adv.*, 2016, **6**, 90846–90855.

25 S. H. Park, A. Roy, S. Beaupré, S. Cho, N. Coates, J. S. Moon, D. Moses, M. Leclerc, K. Lee and A. J. Heeger, *Nat. Photonics*, 2009, **3**, 297.

26 N. C. Giebink, G. P. Wiederrecht, M. R. Wasielewski and S. R. Forrest, *Phys. Rev. B*, 2011, **83**, 195326.

27 K. Sivula, F. Le Formal and M. Gratzel, *ChemSusChem*, 2011, **4**, 432–449.

28 D. Bryant, N. Aristidou, S. Pont, I. Sanchez-Molina, T. Chotchunangatchaval, S. Wheeler, J. R. Durrant and S. A. Haque, *Energy Environ. Sci.*, 2016, **9**, 1655–1660.

29 F. Nour-Mohhamadi, S. D. Nguyen, G. Boschloo, A. Hagfeldt and T. Lund, *J. Phys. Chem. B*, 2005, **109**, 22413–22419.

30 N. J. Turro, *Modern molecular photochemistry*, University science books, 1991.

31 N. J. Turro, V. Ramamurthy and J. C. Scaiano, *Principles of molecular photochemistry: an introduction*, University science books, 2009.

32 A. D. Bandrauk, *Molecules in laser fields*, CRC Press, 1993.

33 B. Valeur and M. N. Berberan-Santos, *Molecular fluorescence: principles and applications*, John Wiley & Sons, 2012.

34 P. Liao and E. A. Carter, *Phys. Chem. Chem. Phys.*, 2011, **13**, 15189–15199.

35 E. Apra, E. A. Carter and A. Fortunelli, *Int. J. Quantum Chem.*, 2004, **100**, 277–287.

36 B. M. Marsh, M. E. Vaida, S. K. Cushing, B. R. Lamoureux and S. R. Leone, *J. Phys. Chem. C*, 2017, **121**, 21904–21912.

37 S. Kucheyev, T. Baumann, P. Sterne, Y. Wang, T. Van Buuren, A. Hamza, L. Terminello and T. Willey, *Phys. Rev. B*, 2005, **72**, 035404.

38 J. Z. Zhang, *Acc. Chem. Res.*, 1997, **30**, 423–429.

39 A. Nilsson, L. G. Pettersson and J. Norskov, *Chemical bonding at surfaces and interfaces*, Elsevier, 2011.

40 G. A. Somorjai and Y. Li, *Proc. Natl. Acad. Sci.*, 2011, **108**, 917.

41 G. A. Somorjai, S. K. Beaumont and S. Alayoglu, *Angew. Chem. Int. Ed.*, 2011, **50**, 10116–10129.

42 L. Liu, Z. Mei, A. Tang, A. Azarov, A. Kuznetsov, Q.-K. Xue and X. Du, *Phys. Rev. B*, 2016, **93**, 235305.

43 T. S. Bjorheim, M. Arrigoni, S. W. Saeed, E. Kotomin and J. Maier, *Chem. Mater.*, 2016, **28**, 1363–1368.

44 M. Fernandez-Serra, C. Adessi and X. Blase, *Phys.Rev.Lett.*, 2006, **96**, 166805.

45 T. Arias and J. Joannopoulos, *Phys. Rev. B.*, 1994, **49**, 4525.

46 M. A. van der Horst and K. J. Hellingwerf, *Acc. Chem. Res.*, 2004, **37**, 13–20.

47 C. T. Middleton, K. de La Harpe, C. Su, Y. K. Law, C. E. Crespo-Hernandez and B. Kohler, *Annu. Rev. Phys. Chem.*, 2009, **60**, 217–239.

48 I. V. Khudyakov, Y. A. Serebrennikov and N. J. Turro, *Chem. Rev.*, 1993, **93**, 537–570.

49 A. J. Esswein and D. G. Nocera, *Chem. Rev.*, 2007, **107**, 4022–4047.

50 S. Sorenson, E. Driscoll, S. Haghighat and J. M. Dawlaty, *J. Phys. Chem. C*, 2014, **118**, 23621–23626.

51 K. Wu, J. Chen, J. R. McBride and T. Lian, *Science*, 2015, **349**, 632–635.

52 N. Song, H. Zhu, Z. Liu, Z. Huang, D. Wu and T. Lian, *ACS Nano*, 2013, **7**, 1599–1608.

53 H. Zhu, J. Wang, Z. Gong, Y. D. Kim, J. Hone and X. Y. Zhu, *Nano Lett.*, 2017, **17**, 3591–3598.

54 D. M. Herlihy, M. M. Waegele, X. Chen, C. Pemmaraju, D. Prendergast and T. Cuk, *Nat. Chem.*, 2016, **8**, 549–555.

55 A. Esser, W. KÃijtt, M. Strahnen, G. Maidorn and H. Kurz, *Appl. Surf. Sci.*, 1990, **46**, 446–450.

56 A. G. Joly, J. R. Williams, S. A. Chambers, G. Xiong, W. P. Hess and D. M. Laman, *J. Appl. Phys.*, 2006, **99**, 053521.

57 H. Q. Doan, K. L. Pollock and T. Cuk, *Chem. Phys. Lett.*, 2016, **649**, 1–7.

58 N. Gedik, J. Orenstein, R. Liang, D. A. Bonn and W. N. Hardy, *Science*, 2003, **300**, 1410–1412.

59 C. M. Sutter-Fella, Y. Li, M. Amani, J. W. Ager, F. M. Toma, E. Yablonovitch, I. D. Sharp and A. Javey, *Nano Lett.*, 2016, **16**, 800–806.

60 W. Tian, R. Cui, J. Leng, J. Liu, Y. Li, C. Zhao, J. Zhang, W. Deng, T. Lian and S. Jin, *Angew. Chem. Int. Ed.*, 2016, **128**, 13261–13265.

61 C. Galland, Y. Ghosh, A. SteinbrÃijck, M. Sykora, J. A. Hollingsworth, V. I. Klimov and H. Htoon, *Nature*, 2011, **479**, 203.

62 A. A. Cordones, T. J. Bixby and S. R. Leone, *Nano Lett.*, 2011, **11**, 3366–3369.

63 M. Cinchetti, K. Heimer, J.-P. WÃijstenberg, O. Andreyev, M. Bauer, S. Lach, C. Ziegler, Y. Gao and M. Aeschlimann, *Nat. Mater.*, 2008, **8**, 115.

64 S. Tan, L. Liu, Y. Dai, J. Ren, J. Zhao and H. Petek, *J. Am. Chem. Soc.*, 2017, **139**, 6160–6168.

65 N.-H. Ge, C. M. Wong and C. B. Harris, *Acc. Chem. Res.*, 2000, **33**, 111–118.

66 Y. Song, C. Hellmann, N. Stingelin and G. D. Scholes, *J. Chem. Phys.*, 2015, **142**, 212410.

67 L. Wang, N. E. Williams, E. W. Malachosky, J. P. Otto, D. Hayes, R. E. Wood, P. Guyot-Sionnest and G. S. Engel, *ACS Nano*, 2017, **11**, 2689–2696.

68 S. D. Park, D. Baranov, J. Ryu, B. Cho, A. Halder, S. Seifert, S. Vajda and D. M. Jonas, *Nano Lett.*, 2017, **17**, 762–771.

69 L. Foglia, M. Wolf and J. Stahler, *Appl. Phys. Lett.*, 2016, **109**, 202106.

70 W. A. Tisdale, M. Muntwiler, D. J. Norris, E. S. Aydil and X. Y. Zhu, *J. Phys. Chem. C*, 2008, **112**, 14682–14692.

71 D. Hayes, R. G. Hadt, J. D. Emery, A. A. Cordones, A. B. Martinson, M. L. Shelby, K. A. Fransted, P. D. Dahlberg, J. Hong, X. Zhang *et al.*, *Energy Environ. Sci.*, 2016, **9**, 3754–3769.

72 M. T. Greiner, M. G. Helander, W.-M. Tang, Z.-B. Wang, J. Qiu and Z.-H. Lu, *Nat. Mater.*, 2012, **11**, 76–81.

73 R. Hoffman, *Solids and surfaces: a chemist's view of bonding in extended structures*, Cornell univ ithaca ny baker lab technical report, 1988.

74 J. Vura-Weis, C.-M. Jiang, C. Liu, H. Gao, J. M. Lucas, F. M. F. de Groot, P. Yang, A. P. Alivisatos and S. R. Leone, *J. Phys. Chem. Lett.*, 2013, **4**, 3667–3671.

75 N. Ansari, K. Ulman, M. F. Camellone, N. Seriani, R. Gebauer and S. Piccinin, *Phys. Rev. Materials*, 2017, **1**, 035404.

76 M. Barroso, C. A. Mesa, S. R. Pendlebury, A. J. Cowan, T. Hisatomi, K. Sivula, M. Gratzel, D. R. Klug and J. R. Durrant, *Proc. Natl. Acad. Sci.*, 2012, **109**, 15640–15645.

77 M. Barroso, S. R. Pendlebury, A. J. Cowan and J. R. Durrant, *Chem. Sci.*, 2013, **4**, 2724–2734.

78 S. R. Pendlebury, X. Wang, F. Le Formal, M. Cornuz, A. Kafizas, S. D. Tilley, M. Gratzel and J. R. Durrant, *J. Am. Chem. Soc.*, 2014, **136**, 9854–9857.

79 S. R. Pendlebury, M. Barroso, A. J. Cowan, K. Sivula, J. Tang, M. Gratzel, D. Klug and J. R. Durrant, *Chem. Commun.*, 2011, **47**, 716–718.

80 C. Bressler and M. Chergui, *Chem.Rev.*, 2004, **104**, 1781–1812.

81 F. de Groot, *Chem. Rev.*, 2001, **101**, 1779–1808.

82 G. Smolentsev and V. Sundstrom, *Coord. Chem. Rev.*, 2015, **304-305**, 117–132.

83 D. Prendergast and G. Galli, *Phys. Rev.Lett.*, 2006, **96**, 215502.

84 X. Liu, J. Liu, R. Qiao, Y. Yu, H. Li, L. Suo, Y.-s. Hu, Y.-D. Chuang, G. Shu, F. Chou, T.-C. Weng, D. Nordlund, D. Sokaras, Y. J. Wang, H. Lin, B. Barbiellini, A. Bansil, X. Song, Z. Liu, S. Yan, G. Liu, S. Qiao, T. J. Richardson, D. Prendergast, Z. Hussain, F. M. F. de Groot and W. Yang, *J. Am. Chem. Soc.*, 2012, **134**, 13708–13715.

85 X. Zhang, G. Smolentsev, J. Guo, K. Attenkofer, C. Kurtz, G. Jennings, J. V. Lockard, A. B. Stickrath and L. X. Chen, *J. Phys. Chem. Lett.*, 2011, **2**, 628–632.

86 M. R. Harpham, S. C. Nguyen, Z. Hou, J. C. Grossman, C. B. Harris, M. W. Mara, A. B. Stickrath, Y. Kanai, A. M. Kolpak, D. Lee *et al.*, *Angew. Chem. Int. Ed.*, 2012, **51**, 7692–7696.

87 M. Khalil, M. A. Marcus, A. L. Smeigh, J. K. McCusker, H. H. Chong and R. W. Schoenlein, *J. Phys. Chem. A*, 2006, **110**, 38–44.

88 K. Tiedtke, A. Azima, N. von Bargen, L. Bittner, S. Bonfigt, S. Dusterer, B. Faatz, U. Fruhling, M. Gensch, C. Gerth, N. Guerassimova, U. Hahn, T. Hans, M. Hesse, K. Honkavaar, U. Jastrow, P. Juranic, S. Kapitzki, B. Keitel, T. Kracht, M. Kuhlmann, W. B. Li, M. Martins, T. Nunez, E. Plonjes, H. Redlin, E. L. Saldin, E. A. Schneidmiller, J. R. Schneider, S. Schreiber, N. Stojanovic, F. Tavella, S. Toleikis, R. Treusch, H. Weigelt, M. Wellhofer, H. Wabnitz, M. V. Yurkov and J. Feldhaus, *New J. Phys.*, 2009, **11**, 023029.

89 C. Gutt, T. Sant, D. Ksenzov, F. Capotondi, E. Pedersoli, L. Raimondi, I. P. Nikolov, M. Kiskinova, S. Jaiswal, G. Jakob, M. Klaeui, H. Zabel and U. Pietsch, *Struct. Dyn.*, 2017, **4**, 055101.

90 C. Bostedt, J. D. Bozek, P. H. Bucksbaum, R. N. Coffee, J. B. Hastings, Z. Huang, R. W. Lee, S. Schorb, J. N. Corlett, P. Denes, P. Emma, R. W. Falcone, R. W. Schoenlein, G. Doumy, E. P. Kanter, B. Kraessig, S. Southworth, L. Young, L. Fang, M. Hoener, N. Berrah, C. Roedig and L. F. DiMauro, *J. Phys. B*, 2013, **46**, 164003.

91 Y. Obara, T. Katayama, Y. Ogi, T. Suzuki, N. Kurahashi, S. Karashima, Y. Chiba, Y. Isokawa, T. Togashi, Y. Inubushi, M. Yabashi, T. Suzuki and K. Misawa, *Opt. Express*, 2014, **22**, 1105–1113.

92 C. J. Milne, T. Schietinger, M. Aiba, A. Alarcon, J. Alex, A. Anghel, V. Arsov, C. Beard, P. Beaud, S. Bettoni *et al.*, *Appl. Sci.*, 2017, **7**, 720.

93 M. Bargheer, N. Zhavoronkov, Y. Gritsai, J. C. Woo, D. S. Kim, M. Woerner and T. Elsaesser, *Science*, 2004, **306**, 1771–1773.

94 K. Sokolowski-Tinten, C. Blome, J. Blums, A. Cavalleri, C. Dietrich, A. Tarasevitch, I. Uschmann, E. Forster, M. Kammler, M. Horn-von Hoegen *et al.*, *Nature*, 2003, **422**, 287.

95 A. Rousse, C. Rischel, S. Fourmaux, I. Uschmann, S. Sebban, G. Grillon, P. Balcou, E. Förster, J.-P. Geindre, P. Audebert *et al.*, *Nature*, 2001, **410**, 65.

96 M. M. Murnane, H. C. Kapteyn, M. D. Rsen and R. W. Falcone, *Science*, 1991, **251**, 531–536.

97 K. Hatanaka, T. Miura and H. Fukumura, *Appl. Phys. Lett.*, 2002, **80**, 3925–3927.

98 J. C. Kieffer, M. Chaker, J. P. Matte, H. Pepin, C. Y. Cote, Y. Beaudoin, T. W. Johnston, C. Y. Chien, S. Coe, G. Mourou and O. Peyrusse, *Phys. Plasmas.*, 1993, **5**, 2676–2681.

99 D. Kiesewetter, R. Jones, A. Camper, S. Schoun, P. Agostini and L. DiMauro, *Nat. Phys.*, 2018, **14**, 68.

100 M. Chini, K. Zhao and Z. Chang, *Nat. Photonics*, 2014, **8**, 178.

101 P. B. Corkum and F. Krausz, *Nat. Phys.*, 2007, **3**, 381.

102 P. M. Paul, E. Toma, P. Breger, G. Mullot, F. Augé, P. Balcou, H. Muller and P. Agostini, *Science*, 2001, **292**, 1689–1692.

103 A. Bhattacherjee, C. D. Pemmaraju, K. Schnorr, A. R. Attar and S. R. Leone, *J. Am. Chem. Soc.*, 2017, **139**, 16576–16583.

104 A. R. Attar, A. Bhattacherjee, C. D. Pemmaraju, K. Schnorr, K. D. Closser, D. Prendergast and S. R. Leone, *Science*, 2017, **356**, 54–59.

105 J. Li, X. Ren, Y. Yin, K. Zhao, A. Chew, Y. Cheng, E. Cunningham, Y. Wang, S. Hu, Y. Wu *et al.*, *Nat. Commun.*, 2017, **8**, 186.

106 C.-M. Jiang, L. R. Baker, J. M. Lucas, J. Vura-Weis, A. P. Alivisatos and S. R. Leone, *J. Phys. Chem. C*, 2014, **118**, 22774–22784.

107 L. R. Baker, C.-M. Jiang, S. T. Kelly, J. M. Lucas, J. Vura-Weis, M. K. Gilles, A. P. Alivisatos and S. R. Leone, *Nano Lett.*, 2014, **14**, 5883–5890.

108 M. Schultze, K. Ramasesha, C. Pemmaraju, S. Sato, D. Whitmore, A. Gandman, J. S. Prell, L. J. Borja, D. Prendergast, K. Yabana, D. M. Neumark and S. R. Leone, *Science*, 2014, **346**, 1348–1352.

109 M. Zurch, H.-T. Chang, L. J. Borja, P. M. Kraus, S. K. Cushing, A. Gandman, C. J. Kaplan, M. H. Oh, J. S. Prell, D. Prendergast *et al.*, *Nat. Commun.*, 2017, **8**, 15734.

110 L. M. Carneiro, S. K. Cushing, C. Liu, Y. Su, P. Yang, A. P. Alivisatos and S. R. Leone, *Nat. Mater.*, 2017, **16**, 819.

111 M. P. Seah and W. Dench, *Surf. Interface Anal.*, 1979, **1**, 2–11.

112 O. Schmidt, M. Bauer, C. Wiemann, R. Porath, M. Scharte, O. Andreyev, G. Schonhense and M. Aeschlimann, *Appl. Phys. B*, 2002, **74**, 223–227.

113 M. J. Ambrosio and U. Thumm, *Phys. Rev. A*, 2016, **94**, 063424.

114 C. Lei, M. Bauer, K. Read, R. Tobey, Y. Liu, T. Popmintchev, M. M. Murnane and H. C. Kapteyn, *Phys. Rev. B*, 2002, **66**, 245420.

115 M. Bauer, C. Lei, K. Read, R. Tobey, J. Gland, M. Murnane and H. Kapteyn, *Phys. Rev. Lett.*, 2001, **87**, 025501.

116 M. E. Vaida and S. R. Leone, *J. Phys. Chem. C*, 2016, **120**, 2769–2776.

117 M. Chergui and E. Collet, *Chem. Rev.*, 2017, **117**, 11025–11065.

118 W. Gawelda, M. Johnson, F. M. de Groot, R. Abela, C. Bressler and M. Chergui, *J. Am. Chem. Soc.*, 2006, **128**, 5001–5009.

119 G. B. Shaw, C. D. Grant, H. Shirota, E. W. Castner, G. J. Meyer and L. X. Chen, *J. Am. Chem. Soc.*, 2007, **129**, 2147–2160.

120 C. Liu, J. Zhang, L. M. Lawson Daku, D. Gosztola, S. E. Canton and X. Zhang, *J. Am. Chem. Soc.*, 2017, **139**, 17518–17524.

121 A. Cirri, J. Husek, S. Biswas and L. R. Baker, *J. Phys. Chem. C*, 2017, **121**, 15861–15869.

122 J. Husek, A. Cirri, S. Biswas and L. R. Baker, *Chem. Sci.*, 2017, **8**, 8170–8178.

123 S. Biswas, J. Husek, S. Londo and L. R. Baker, *Nano Lett.*, 2018, **18**, 1228–1233.

124 B. L. Henke, E. M. Gullikson and J. C. Davis, *At. Data Nucl. Data Tables*, 1993, **54**, 181–342.

125 E. Stavitski and F. M. De Groot, *Micron*, 2010, **41**, 687–694.

126 D. J. Griffiths, *Introduction To Electrodynamics (1989)*.

127 R. Berlasso, C. Dallera, F. Borgatti, C. Vozzi, G. Sansone, S. Stagira, M. Nisoli, G. Ghiringhelli, P. Villoresi, L. Poletto, M. Pascolini, S. Nannarone, S. D. Silvestri and L. Braicovich, *Phys. Rev. B*, 2006, **73**, 115101.

128 N. Safta, J.-P. Lacharme, C. Sébenne and A. Akremi, *J. Phys. Condens. Matter*, 1993, **5**, 6623.

129 F. Theilmann, R. Matzdorf, G. Meister and A. Goldmann, *Phys. Rev. B*, 1997, **56**, 3632.

130 R. Kostecki and J. Augustynski, *J. Appl. Phys.*, 1995, **77**, 4701–4705.

131 S. Shen, S. A. Lindley, X. Chen and J. Z. Zhang, *Energy Environ. Sci.*, 2016, **9**, 2744–2775.

132 F. Le Formal, N. Tetreault, M. Cornuz, T. Moehl, M. Gratzel and K. Sivula, *Chem. Sci.*, 2011, **2**, 737–743.

133 A. J. Rettie, W. D. Chemelewski, D. Emin and C. B. Mullins, *J. Phys. Chem. Lett.*, 2016, **7**, 471–479.

134 T. J. Smart and Y. Ping, *J. Phys. Condens. Matter.*, 2017, **29**, 394006.

135 N. Li, D. K. Bediako, R. G. Hadt, D. Hayes, T. J. Kempa, F. von Cube, D. C. Bell, L. X. Chen and D. G. Nocera, *Proc. Natl. Acad. Sci.*, 2017, **114**, 1486–1491.

136 Z. Wang and K. H. Bevan, *Phys. Rev. B*, 2016, **93**, 024303.

137 N.-H. Ge, C. Wong, R. Lingle, J. McNeill, K. Gaffney and C. Harris, *Science*, 1998, **279**, 202–205.

138 M. Muntwiler and X.-Y. Zhu, *Phys. Rev. Lett.*, 2007, **98**, 246801.

139 T. Wang, C. Caraiani, G. W. Burg and W.-L. Chan, *Phys. Rev. B*, 2015, **91**, 041201.

140 J. P. Toennies, *Superlattices Microstruct.*, 1990, **7**, 193–200.

141 M. J. Lagos, A. Trügler, U. Hohenester and P. E. Batson, *Nature*, 2017, **543**, 529.

142 H. Lourenço-Martins and M. Kociak, *Phys. Rev. X*, 2017, **7**, 041059.

143 B. Klahr, S. Gimenez, F. Fabregat-Santiago, T. Hamann and J. Bisquert, *J. Am. Chem. Soc.*, 2012, **134**, 4294–4302.

144 F. Le Formal, E. Pastor, S. D. Tilley, C. A. Mesa, S. R. Pendlebury, M. GraĬLtzel and J. R. Durrant, *J. Am. Chem. Soc.*, 2015, **137**, 6629–6637.

145 F. Jiao and H. Frei, *Angew. Chem. Int. Ed.*, 2009, **48**, 1841–1844.

146 Z. Su, J. S. Baskin, W. Zhou, J. M. Thomas and A. H. Zewail, *J. Am. Chem. Soc.*, 2017, **139**, 4916–4922.

147 F. M. F. de Groot, M. Grioni, J. C. Fuggle, J. Ghijsen, G. A. Sawatzky and H. Petersen, *Phys. Rev. B*, 1989, **40**, 5715–5723.

148 J. Suntivich, W. T. Hong, Y.-L. Lee, J. M. Rondinelli, W. Yang, J. B. Goodenough, B. Dabrowski, J. W. Freeland and Y. Shao-Horn, *J. Phys. Chem. C*, 2014, **118**, 1856–1863.

149 M.-F. Lin, M. A. Verkamp, J. Leveillee, E. S. Ryland, K. Benke, K. Zhang, C. Weninger, X. Shen, R. Li, D. Fritz, U. Bergmann, X. Wang, A. Schleife and J. Vura-Weis, *J. Phys. Chem. C*, 2017, **121**, 27886–27893.

150 W. T. Hong, R. E. Welsch and Y. Shao-Horn, *J. Phys. Chem. C*, 2015, **120**, 78–86.

151 C. C. McCrory, S. Jung, I. M. Ferrer, S. M. Chatman, J. C. Peters and T. F. Jaramillo, *J. Am. Chem. Soc*, 2015, **137**, 4347–4357.

152 F. Morin, *Phys. Rev.*, 1954, **93**, 1199.

153 F. Morin, *Phys. Rev.*, 1954, **93**, 1195.

154 N. J. Cherepy, D. B. Liston, J. A. Lovejoy, H. Deng and J. Z. Zhang, *J. Phys. Chem. B*, 1998, **102**, 770–776.

155 J. Chmeliov, J. Narkeliunas, M. W. Graham, G. R. Fleming and L. Valkunas, *Nanoscale*, 2016, **8**, 1618–1626.

156 D. Sun, Y. Rao, G. A. Reider, G. Chen, Y. You, L. BrÃľzin, A. R. Harutyunyan and T. F. Heinz, *Nano Lett.*, 2014, **14**, 5625–5629.

157 N. Kumar, Q. Cui, F. Ceballos, D. He, Y. Wang and H. Zhao, *Phys. Rev. B*, 2014, **89**, 125427.

158 P. D. Cunningham, K. M. McCreary and B. T. Jonker, *J. Phys. Chem. Lett.*, 2016, **7**, 5242–5246.

7 Biographies

Somnath Biswas received a BSc degree from Ramakrishna Mission Vidyamandira (Belur, India) in 2013. He obtained a MSc degree from Indian Institute of Technology (Kanpur, India) under the supervision of Pratik Sen in 2015. Currently he is a graduate research associate, pursuing PhD under the supervision of L. Robert Baker at the Ohio State University. His research primarily focuses on ultrafast charge-carrier dynamics at the surface and interface of catalytic materials using time-resolved XUV Reflection-Absorption spectroscopy.

Jakub Husek is a Czech native who received a BS degree in Chemistry from Susquehanna University in 2014 under the supervision of Prof. Dougherty. Currently he is a fourth-year graduate student in the Baker group where he worked on constructing the XUV spectrometer described here. His thesis work has focused on femtosecond surface electron dynamics of functional materials using XUV Reflection-Absorption spectroscopy.

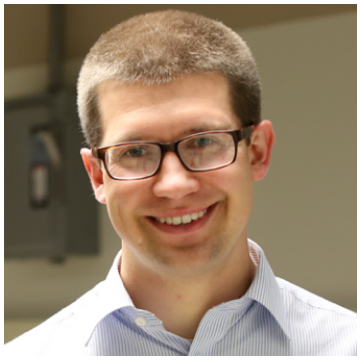

Robert Baker received a BS degree from Brigham Young University in 2007 and a MS degree from Brigham Young University in 2008. He received his PhD from the University of California, Berkeley under the supervision of Gabor Somorjai in 2012. Following his PhD he performed postdoctoral research with Stephen Leone before joining The Ohio State University as an assistant professor in 2014. His research interests are in ultrafast spectroscopy, heterogeneous catalysis, and surface science. He is a recipient of the Air Force Office of Scientific Research Young Investigator Award and the Department of Energy Early Career Award.

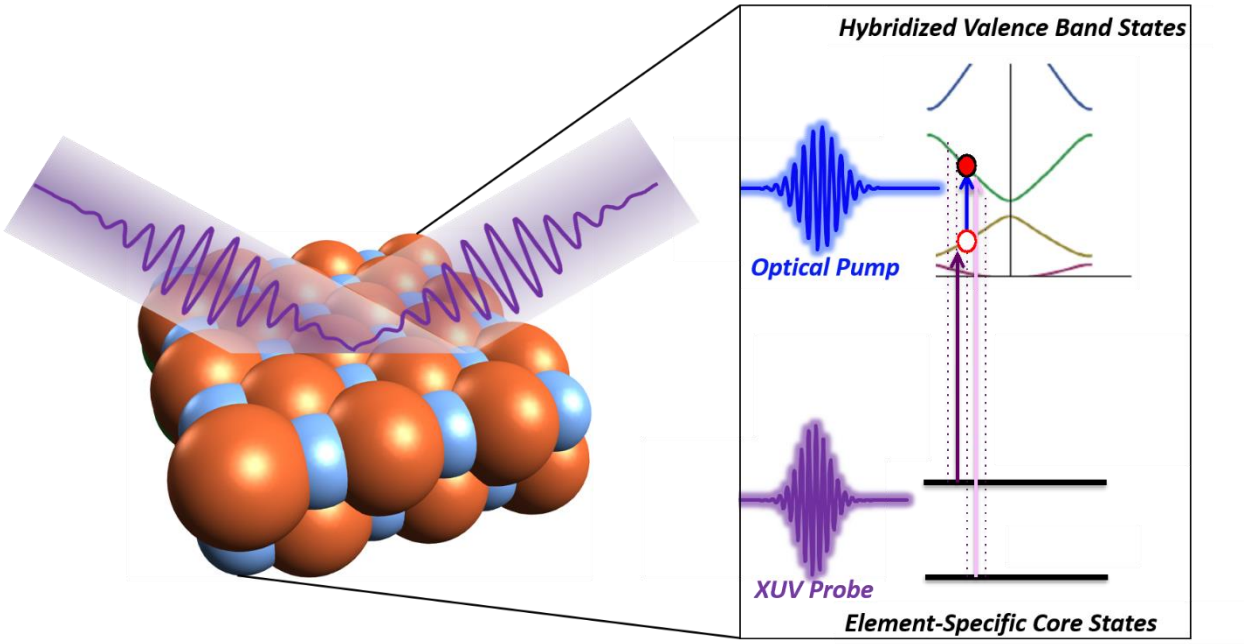

Time-Resolved XUV reflection-absorption spectroscopy probes core-to-valence transitions to reveal state-specific electron dynamics at surfaces.